Mixed-dimensional moiré systems of twisted graphitic thin films

Dacen Waters[1,2*], Ellis Thompson[1*], Esmeralda Arreguin-Martinez[3], Manato Fujimoto[4,3], Yafei Ren[3], Kenji Watanabe[5], Takashi Taniguchi[6], Ting Cao[3], Di Xiao[3,1], and Matthew Yankowitz[1,3†]

[1] *Department of Physics, University of Washington, Seattle, Washington, 98195, USA*

[2] *Intelligence Community Postdoctoral Research Fellowship Program, University of Washington, Seattle, Washington, 98195, USA*

[3] *Department of Materials Science and Engineering, University of Washington, Seattle, Washington, 98195, USA*

[4] *Department of Physics, Osaka University, Osaka 560-0043, Japan*

[5] *Research Center for Functional Materials, National Institute for Materials Science, 1-1 Namiki, Tsukuba 305-0044, Japan*

[6] *International Center for Materials Nanoarchitectonics, National Institute for Materials Science, 1-1 Namiki, Tsukuba 305-0044, Japan*

[*] *These authors contributed equally to this work. and*

[†] *myank@uw.edu (M.Y.)*

Moiré patterns formed by stacking atomically-thin van der Waals crystals with a relative twist angle can give rise to dramatic new physical properties [1, 2]. The study of moiré materials has so far been limited to structures comprising no more than a few vdW sheets, since a moiré pattern localized to a single two-dimensional interface is generally assumed to be incapable of appreciably modifying the properties of a bulk three-dimensional crystal. Here, we perform transport measurements of dual-gated devices constructed by slightly rotating a monolayer graphene sheet atop a thin bulk graphite crystal. We find that the moiré potential transforms the electronic properties of the entire bulk graphitic thin film. At zero and small magnetic fields, transport is mediated by a combination of gate-tunable moiré and graphite surface states, as well as coexisting semimetallic bulk states that do not respond to gating. At high field, the moiré potential hybridizes with the graphitic bulk states owing to the unique properties of the two lowest Landau bands of graphite. These Landau bands facilitate the formation of a single quasi–two-dimensional hybrid structure in which the moiré and bulk graphite states are inextricably mixed. Our results establish twisted graphene-graphite as the first in a new class of mixed-dimensional moiré materials.

Twisting two sheets of monolayer graphene by a small angle results in the formation of a long-wavelength moiré potential that substantially alters the low-energy bands [3, 4]. The moiré bands become extremely flat and isolated near the "magic angle" of approximately 1.1°, generating an array of strongly correlated states including magnetism and superconductivity [1, 2, 5–8]. Moiré flat bands also form upon incorporating additional graphene sheets into the structure, recently observed in the magic-angle trilayer/tetralayer/pentalayer family [9–13] as well as in twisted monolayer-bilayer [14–17] and bilayer-bilayer graphene [18–22]. So far, the study of twisted graphene structures has mostly been limited to those assembled from monolayer and bilayer graphene building blocks, since thicker Bernal-stacked constituents contribute additional bands at low energy. Band structure modeling [23] and scanning tunneling microscopy studies of rotationally-faulted graphite [24] indicate that moiré bands are likely to persist to arbitrarily thick Bernal graphite structures, but remain localized at the twisted interface and coexist with conventional bulk graphite bands. However, it is currently not known whether and how these moiré surface states impact the electronic properties of the entire bulk graphitic thin film.

Here, we investigate the transport properties of graphitic structures with a moiré interface created by a single rotational fault within the crystal. We primarily focus on the case where the moiré potential is localized to one surface of the structure, achieved by rotating a flake of monolayer graphene by a small twist angle atop a Bernal graphite thin film. We also compare to the case where the moiré interface is buried at the center of the graphitic structure. We show that a single two-dimensional moiré interface can strongly modify the properties of the entire graphitic thin film, owing to a number of unique properties arising from its semimetallic nature.

Transport in Bernal and moiré graphite

We focus our study primarily on twisted graphene-graphite (i.e., t1+Z, where 1 indicates monolayer graphene and Z corresponds to the number of graphene sheets in the bulk thin film). We first compare the transport properties of Bernal graphite with a representative twisted graphene-graphite device. Figure 1 shows this for the case of a 23-layer Bernal graphite device and a t1+10 device with $\theta = 0.84°$. A schematic of the Bernal graphite device is shown in Fig. 1a, with top and bottom gate voltages denoted as V_t and V_b, respectively.

The color map in Fig. 1b shows the longitudinal resistance, R_{xx}, of the device at zero magnetic field as a

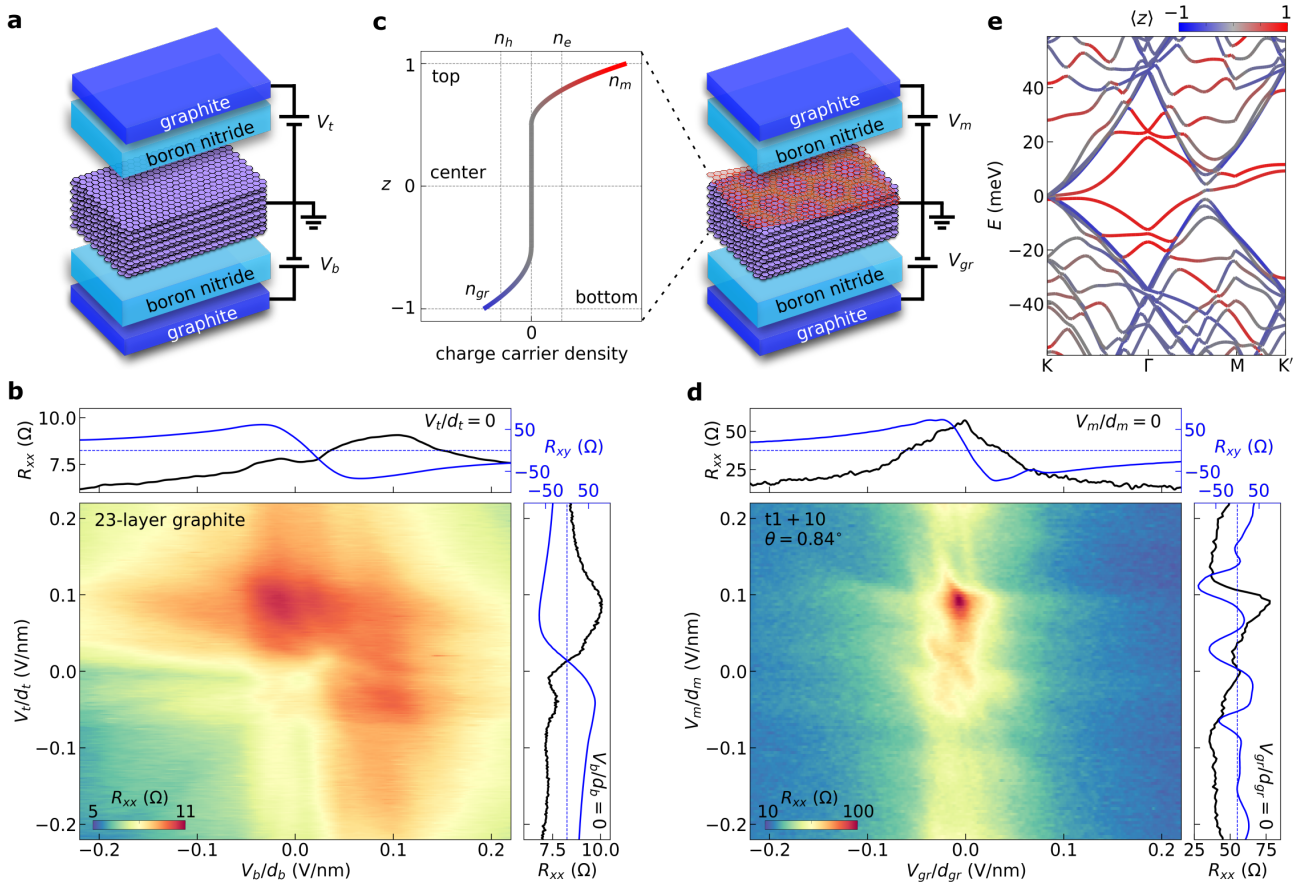

FIG. 1. **Comparison of Bernal and moiré graphite at zero field. a**, Cartoon schematic of a Bernal graphite thin film device with top (V_t) and bottom (V_b) gates. **b**, Resistance of a 23-layer Bernal graphite thin film as a function of the top and bottom gate voltages. The top (bottom) gate voltage is normalized by the top (bottom) BN thickness, d_t (d_b). The panel above (to the right) of the color map shows cuts of R_{xx} and R_{xy} as V_b (V_t) is swept with $V_t = 0$ ($V_b = 0$). R_{xy} is acquired with $B = 0.2$ T. **c**, (Right) Cartoon schematic of a moiré graphite thin film device. The gate facing the moiré (Bernal graphite) surface is denoted V_m (V_{gr}). (Left) Schematic illustration of the free charge distribution in a dual-gated graphitic thin film as a function of the position along the c-axis of graphite (denoted as z). n_m and n_{gr} are the charge carrier densities on the moiré and Bernal graphite surfaces, respectively. These can be modified by tuning V_m and V_{gr}, shown here with arbitrarily chosen magnitudes and signs. n_e and n_h denote the density of electron and hole carriers in graphite, which are approximately equal such that the total doping is zero in the bulk. The doping in the bulk does not depend on gating. **d**, Resistance of a t1+10 graphite sample with $\theta = 0.84°$ as a function of V_m and V_{gr}, normalized by the appropriate BN thicknesses. The panels above and to the right of the color map show cuts of R_{xx} and R_{xy}, analogous to those in **b**. **e**, Calculation of the band structure of a t1+10 graphite sample with $\theta = 0.84°$. The cut is taken along a contour within the moiré Brillouin zone. The color of bands corresponds to their expectation value along the graphite c-axis, denoted as ⟨z⟩, where a value of 1 (-1) corresponds to the moiré (Bernal graphite) surface as shown in **c**.

function of the voltage on both gates (each gate voltage is normalized by the corresponding BN dielectric thickness). The resistance changes by only a few ohms with gating, consistent with the expectation that the gates are only able to dope the outer few layers of the nearest graphite surface due to screening in the bulk. Consequentially, the primary resistance features we observe evolve either vertically or horizontally in the map. This can also be seen by comparing the black traces in the panels above and to the right of the resistance map, which show R_{xx} as each gate is swept with the other held at ground. We further see corroborating behavior in the Hall resistance, R_{xy}, measured in a small magnetic field of $B = 0.2$ T. In particular, R_{xy} exhibits a sign change around zero bias in each gate sweep, signifying a corresponding sign change in the charge of the free carriers residing in the surface accumulation layer.

In contrast to our observations in Bernal graphite, transport in our t1+10 sample differs considerably depending on which gate is swept, as the mirror symmetry of the structure is broken by the rotated graphene sheet at the surface. Here, we denote the voltage on the gate

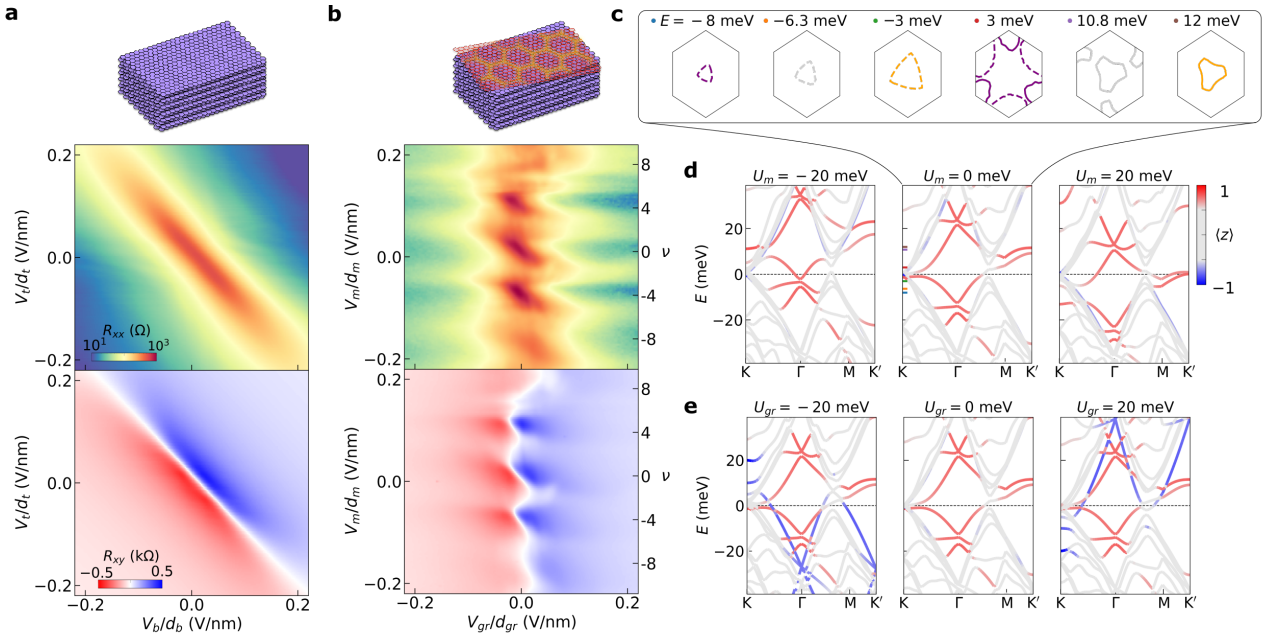

FIG. 2. **Low-field magnetotransport and independent gating of surface-localized states.** **a**, Longitudinal (top) and Hall (bottom) resistance maps of the 23-layer Bernal graphite device acquired at $B = 0.5$ T. **b**, The same maps acquired in the t1+10 moiré graphite device. The vertical axis on the right indicates the filling factor, ν, of the moiré surface bands. The Hall resistance maps in **a-b** are antisymmetrized. Schematics of the Bernal graphite and t1+10 graphite are shown above each of the corresponding R_{xx} maps. **c**, Constant-energy contours of the surface-localized moiré bands at the denoted energies, calculated without any applied gate voltage (i.e., $U_m = U_{gr} = 0$). Dashed (solid) lines denote contours from the moiré valence (conduction) band. Energy labels for each panel have color-coded dots corresponding to the tick marks in **d**. Contours are color-coded by the sign of the local moiré band curvature, with orange denoting a hole-like Fermi surface, purple denoting an electron-like Fermi surface, and gray denoting a saddle point. The solid hexagon denotes the moiré Brillouin zone. **d**, Calculation of the band structure of a t1+10 graphite sample with $\theta = 0.84°$ as the surface potential at the moiré interface is changed from $U_m = -20$ meV (left) to 0 (center) to +20 meV (right). The potential at the Bernal graphite surface is $U_{gr} = 0$. The Fermi energy is held fixed at zero energy (black dashed line). The potential drop across graphite layers is modeled using a Thomas-Fermi screening approximation (see Methods). **e**, The same calculation but with $U_m = 0$ and a varying U_{gr}. In **d-e**, the bands are color-coded according to the expectation value of their z coordinate along the c-axis of the graphitic structure.

facing the moiré (Bernal graphite) surface as V_m (V_{gr}) (see Fig. 1c). We see a much larger change in the resistance with gating in this device (Fig. 1d), with the highest resistance confined to a small region around $V_{gr} \approx 0$. Transport is reminiscent of Bernal graphite when sweeping V_{gr} (see R_{xx} and R_{xy} traces in the top panel), but exhibits fundamentally new behavior when sweeping V_m (right panel). In particular, repeated R_{xy} sign changes indicate multiple instances in which the free carriers on the twisted surface switch between electron- and hole-like. This behavior arises from the moiré reconstruction of the graphite band structure, marking the formation of a series of surface-localized moiré bands. These can be seen in calculations of the band structure of this material (Fig. 1e, see Methods for details). The bands are color-coded based upon their expectation value along the graphite c-axis, denoted as ⟨z⟩, where a value of 1 (-1) corresponds to the moiré (Bernal graphite) surface. We find moiré bands localized on the outer graphene layers at the rotated interface (red colored bands), consistent with previous calculations performed for infinitely thick graphite slabs [23].

The contrast between Bernal and moiré graphite becomes more obvious upon applying a small magnetic field oriented along the c-axis. Figure 2a shows a dual-gate resistance map for the 23-layer Bernal graphite sample acquired at a magnetic field of $B = 0.5$ T. The resistance is largest when the voltage on both gates is approximately zero, consistent with prior reports of a large magnetoresistance (MR) in bulk graphite crystals [25]. Upon gating, we additionally find a large MR everywhere along the condition of overall charge neutrality, $V_t/d_t + V_b/d_b = 0$, as evidenced by the diagonal resistance stripe in Fig. 2a. Measurements of the Hall resistance show a corresponding sign change across the line of overall neutrality. Our observations can be captured by a simple Drude transport model (see Methods and Supplementary Information Fig. S8), indicating that transport is primarily determined by the total free charge density in the material, even when the gate-induced charge is mostly localized at the outer surfaces (see Fig. 1c).

Corresponding measurements of the moiré sample re-

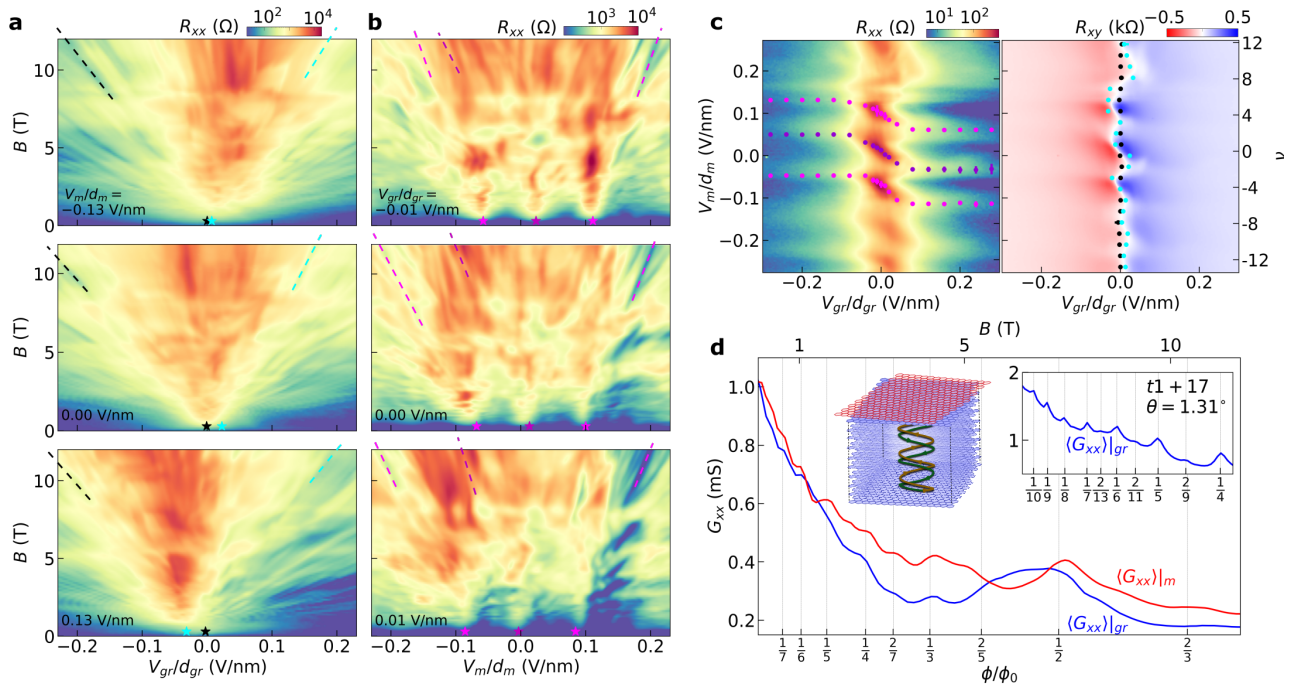

FIG. 3. **Hybridization of moiré and bulk graphite states at high field. a**, Landau fan diagrams from the t1+10 device acquired by sweeping V_{gr} at the denoted values of V_m. The black dashed lines indicate selected QOs that project to $V_{gr} \approx 0$ at $B = 0$, whereas the blue dashed lines denote QOs that project to a value of V_{gr} that changes with V_m. **b**, Landau fan diagrams acquired by sweeping V_m at the denoted values of V_{gr}. The purple dashed lines indicate selected QOs that project to $\nu = 0$, whereas the pink dashed lines indicate QOs that project to $\nu = \pm 4$. **c**, Longitudinal (left) and Hall (right) resistance maps acquired at $B = 0.5$ T. Zero-field projections of the $\nu = 0$ and ± 4 states from the moiré gate Landau fans are overlaid on the longitudinal resistance map. Zero-field projections of QOs from the graphite gate Landau fans are overlaid on the Hall resistance map. Supplementary Videos 1-2 show the Landau fan diagrams used to extract all of the data points. **d**, Conductance, G_{xx}, as a function of magnetic field. The blue (red) line is averaged over all values of V_{gr} (V_m) for the Landau fan corresponding to the top panel in **a** (**b**), thereby eliminating contributions from individual QOs at a given field. Selected rational values of the magnetic flux filling of the moiré unit cell, ϕ/ϕ_0 are denoted by vertical gray lines. The top right inset shows G_{xx} averaged over all values of V_{gr} for a t1+17 device with $\theta = 1.31°$ (see Extended Data Fig. 2 for the complete data set from this device). The top left inset shows a cartoon schematic illustrating the formation of a standing wave in the lowest Landau bands of graphite (formed by the stacked blue graphene sheets) at high field. The standing wave hybridizes the Bernal graphite bulk states with the moiré surface states. The moiré interface is indicated by the rotated graphene sheet colored in red.

veal a more complex dependence of transport on gating (Fig. 2b and Extended Data Fig. 1). Rather than a single resistance stripe, R_{xx} exhibits a maximum that evolves with a peculiar zig-zag trajectory upon gating. The contour of $R_{xy} = 0$ tracks closely with the R_{xx} maximum. Notably, the periodic resets we observe upon biasing V_m correspond closely with integer multiples of the gate voltage required to completely fill the four-fold degenerate surface moiré minibands, denoted by the band filling factor, ν, on the right-hand axis (see Methods for definition of ν).

To understand this behavior, we calculate the band structure of twisted graphene-graphite with tunable gate-induced surface potentials (see Methods for full details). Figures 2c-d show the evolution of the band structure for various values of the potential at the moiré surface, U_m. We find that gating primarily changes the energy of the moiré-like surface states, whereas the graphite-like states in the bulk remain at fixed energy. In contrast, the energy of the moiré-like bands remains fixed upon changing the potential at the Bernal graphite surface, U_{gr}, as shown in Fig. 2e. From this, we can generalize the transport properties of Bernal graphite to the moiré sample. The local behavior surrounding $V_{gr} \approx V_m \approx 0$ is similar for the two structures. However, whereas both surfaces of Bernal graphite can be doped with arbitrarily large densities of either electrons or holes, the twisted surface of the moiré sample hosts a series of narrow flat bands

in which the free charge switches periodically between electron- and hole-like (Fig. 2c). When V_m corresponds to full filling of the moiré band ($\nu = \pm 4$), the surface free charge density returns to approximately zero, and the transport once again mimics the case of undoped Bernal graphite. In the Methods section, we provide additional details of the formation of the zig-zag structure.

Hybridization of moiré and bulk states

So far, we have found that the charge accumulation layers on the two surfaces do not directly hybridize with each other, and are thus controlled independently by the nearest gate. However, this behavior is known to break down in Bernal graphite at higher magnetic fields [26]. In the ultra-quantum limit, only the two lowest (nearly-degenerate) Landau bands cross the Fermi energy, and the electron motion is primarily limited to the c-axis [26, 27]. Electrons form a set of standing waves that penetrate across the entire bulk owing to the quasi-1D nature of these Landau bands. These states are thus controlled equally by the top and bottom gates. All other Landau bands are gapped within the bulk, and although they can be populated at the surfaces by gating, they form a screening layer and can only be controlled by the nearest gate. As a consequence, we find that Landau fans acquired by sweeping a single gate exhibit two distinct sets of quantum oscillations (QOs). One sequence projects to approximately zero gate voltage at $B = 0$, irrespective of the bias applied to the other gate. These QOs correspond to surface-localized states. The second sequence projects to a non-zero gate voltage determined by the bias applied to the opposite gate, in particular following a line of constant overall doping. These QOs correspond to states that are extended across the entire bulk (Extended Data Fig. 3).

The moiré surface states in t1+Z graphite form Hofstadter bands at high field [28], which must smoothly evolve into the Bernal graphite Landau bands in the bulk. Despite this additional complexity, our magnetotransport measurements reveal that ungapped bulk states remain extended across the entire sample. These extended states appear as diagonal features in dual-gate maps taken at fixed magnetic field, confirming their dependence on both gate voltages (Extended Data Fig. 4). We further probe these extended states by acquiring Landau fan diagrams while sweeping V_{gr} at various fixed values of V_m (Fig. 3a). Similar to our observations in Bernal graphite, we see two distinct sequences of QOs that project to different values of V_{gr} at $B = 0$. Selected QOs from the sequence corresponding to states localized at the Bernal graphite surface are denoted by black dashed lines, and project to $V_{gr} \approx 0$ irrespective of V_m. In contrast, the QOs corresponding to the bulk extended states (denoted by blue dashed lines) project to different values of V_{gr} depending sensitively on V_m.

Figure 3c shows the color-coded projections from many Landau fan diagrams overlaid atop the R_{xy} map acquired at $B = 0.5$ T (see Methods and Extended Data Fig. 5 for details of the fitting procedure used to extract the projection points). The projection point of the extended states (blue dots) oscillates with V_m, tracking closely with the $R_{xy} = 0$ contour measured at low field. This behavior is enabled by the unique nature of the extended standing wave states in Bernal graphite. As illustrated schematically in the top left inset of Fig. 3d, the standing wave hybridizes the moiré surface states with the graphite bulk states, inextricably mixing them together. The low- and high-field zig-zag features we see in Fig. 3c arise from distinct physical mechanisms, yet exhibit remarkably consistent behavior that is primarily determined by the total gate-induced free charge in the sample.

Unlike in Bernal graphite, the Landau fan diagrams in twisted grahene-graphite differ substantially depending on which gate is swept. In particular, we see QOs corresponding to the moiré bands only upon sweeping V_m (Fig. 3b). We denote selected QOs projecting to full-filling of the moiré surface bands ($\nu = \pm 4$) with pink dashed lines, whereas QOs projecting to the charge neutrality point ($\nu = 0$) are denoted in purple. Figure 3c shows the $B = 0$ projection points of these states overlaid atop the R_{xx} map acquired at $B = 0.5$ T. The low-field transport around $V_{gr} \approx 0$ exhibits diagonal resistance features closely matching the evolution of the projection points of the high-field QOs at $\nu = 0$ and ± 4. We also find that both the resistance and the QO projections depend only weakly on V_{gr} as the bias is raised further. These observations suggest that the moiré bands can be doped by changing V_{gr} when the bias is small, but that surface states on the Bernal face screen the effect of changing V_{gr} when the bias is large.

Despite the obvious differences in the Landau fan diagrams acquired by sweeping each gate, Brown-Zak (BZ) oscillations [28–33] appear in both. The BZ oscillations correspond to conditions in which charge carriers experience zero effective magnetic field, and thus exhibit straight trajectories in real space [33]. These oscillations occur as maxima in the magnetoconductance, $G_{xx} = R_{xx}/(R_{xx}^2 + R_{xy}^2)$, and arise at rational values of the magnetic flux filling of the moiré unit cell. BZ oscillations are anticipated when sweeping V_m (red curve in Fig. 3d), since charge carriers are directly populating the moiré bands. In contrast, the BZ oscillations seen upon sweeping V_{gr} (blue line in Fig. 3d) are more surprising, since this gate does not directly fill the moiré bands. This effect is more clearly visible in a t1+17 device with $\theta = 1.31°$, which exhibits very sharp magnetoconductance peaks averaged over V_{gr} (top right inset of Fig. 3d).

Although it is possible for the moiré to propagate through bulk graphite due to structural relaxations, this effect has been found to arise only at ultra-small twist angles [34], and is therefore unlikely to be relevant in

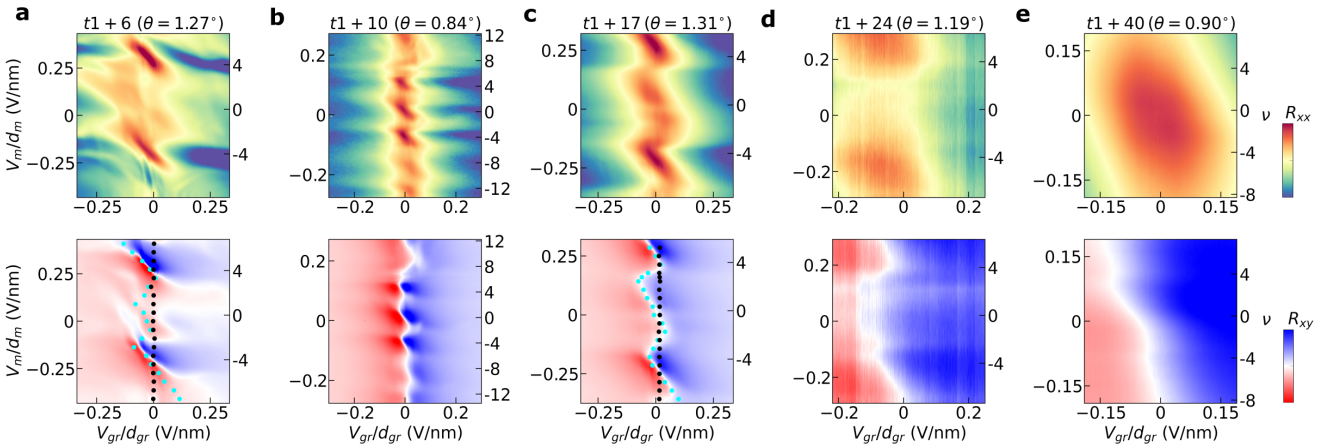

FIG. 4. **Moiré modification of graphitic films with varying thickness and twist angle. a-e**, Maps of the longitudinal (top row) and Hall (bottom row) resistance for different moiré graphite devices, acquired at $B = 0.5$ T. All R_{xy} maps are antisymmetrized, except for that of the t1+40 device. The graphite thickness and twist angle is indicated above each plot. Zero-field projections of QOs from the Landau fans acquired by sweeping V_{gr} are overlaid on the Hall resistance map in **a** and **c**. The extrema of the color scales for each device vary due to the differing graphite thicknesses. The R_{xx} maps are plotted on logarithmic color scales, with extrema of: (**a**) 50 Ω to 1 kΩ, (**b**) 5 Ω to 500 Ω (**c**) 10 Ω to 500 Ω, (**d**) 100 Ω to 175 Ω, (**e**) 50 Ω to 150 Ω. The R_{xy} maps are plotted on linear color scales, with extrema of: (**a**) −0.5 kΩ to 0.5 kΩ, (**b-c**) −0.3 kΩ to 0.3 kΩ, (**d-e**) −50 Ω to 50 Ω.

our samples. Instead, the observation of BZ oscillations upon sweeping V_{gr} indicates that carriers doped into the Bernal graphite surface obey transport properties dictated in part by the moiré potential on the opposite surface, providing further evidence of the hybridization of moiré and bulk states at high field. We additionally find that this effect persists in devices where the moiré interface is buried at the center of the sample (Extended Data Fig. 6). In this case, the moiré bands lie deep in the bulk and can not be filled by either gate, but nevertheless generate strong BZ oscillations by hybridizing with the bulk states of each rotated Bernal graphite constituent.

Discussion

Our observations appear to be generic for t1+Z graphite, as we see qualitative similarities across different graphite thicknesses and twist angles. Figure 4 shows R_{xx} and R_{xy} maps acquired at $B = 0.5$ T for five samples with Bernal graphite components ranging from $Z = 6$ to 40 layers. The zig-zag resistance feature becomes increasingly obscured for thicker graphite, but we nevertheless see oscillations in R_{xy} that appear to correspond closely with four-fold multiples of ν. In the high-field regime, we see a similar evolution of the Landau fan diagram projections for both the t1+6 and t1+17 samples. The projection points from the Landau fans acquired by sweeping V_{gr} are plotted on the corresponding R_{xy} maps shown in Fig. 4a and c, and exhibit a familiar zig-zag progression. The full set of QO projections are shown in Extended Data Figs. 2 and 7, as well as in Supplementary Videos S3-S5.

Overall, our results establish a new class of 'mixed-dimensional moiré materials,' in which a moiré potential localized to a single 2D interface fundamentally transforms the properties of an entire bulk crystal. This behavior may generalize to other layered semimetals with low intrinsic bulk doping, such as WTe_2 or $ZrTe_5$. Our work additionally motivates experiments with more complex graphitic structures, in which bulk standing waves couple moiré patterns at both the top and bottom surfaces or distributed throughout the bulk of the material. The standing-wave coupling may also be exploited to enable other means of interfacial engineering; for instance, by extending proximity-induced superconductivity, magnetism, or spin-orbit coupling into the graphite bulk. Finally, new complex moiré geometries in bulk graphitic thin films may help to unravel the origin of the superconductivity found both in natural few-layer graphene allotropes [35, 36] and in a growing family of magic-angle twisted graphene structures.

METHODS

Device fabrication. Moiré devices were fabricated using the "cut-and-stack" method [37, 38]. t1+Z structures are made by finding an exfoliated bulk graphite thin film with a connected monolayer graphene region, isolating the two using an atomic force microscope tip, and then stacking one atop the other at the desired twist angle. The sample with the buried moiré was made by isolating two regions from a single 7-layer graphite sheet and stacking them atop each other. The samples were assembled using standard dry-transfer techniques with

a polycarbonate (PC)/polydimethyl siloxane (PDMS) stamp [39]. All devices are encapsulated in flakes of BN and graphite, and then transferred onto a Si/SiO_2 wafer. The only exception is the t1+6 device, which has a metal top gate instead of graphite. The temperature was kept below 180°C during device fabrication to preserve the intended twist angle. The number of graphite layers in each device, Z, was determined by atomic force microscopy measurements after encapsulation. Standard electron beam lithography, CHF_3/O_2 plasma etching, and metal deposition techniques (Cr/Au) were used to define the complete stack into a Hall bar geometry [39]. Optical micrographs of all devices are shown in Supplementary Information Fig. S1. We measure devices with graphite thickness varying from $Z = 6$ to 40 layers, and with twist angles between $\theta = 0.84°$ and $1.31°$.

Transport measurements. Transport measurements were performed in a Cryomagnetics variable temperature insert with a base temperature of 1.7 K, and were conducted in a four-terminal geometry with a.c. current excitation of 10-200 nA using standard lock-in techniques at a frequency of 17.7 Hz. Some of the measurements acquired for the Supplementary Videos S1-S2 for the t1+10 device were performed in a Bluefors dilution refrigerator at a nominal base temperature of 20 mK. Antisymmetrization of R_{xy} is performed following $R_{xy} = (R_{xy}[B] - R_{xy}[-B])/2)$.

Twist angle determination. The twist angle θ is determined by fitting the sequence of QOs arising upon sweeping V_m. The charge carrier density required to fill the moiré superlattice is given by $n_s = 8\theta^2/\sqrt{3}a^2$, where $a = 0.246$ nm. The value of n_s is determined by tracing the QOs corresponding to full filling of the moiré surface bands to $B = 0$. The band filling factor, ν, is defined such that $\nu = \pm 4$ at doping $\pm n_s$, where the numerical factor of 4 corresponds to the spin and valley degeneracy of graphene. We note that the value of V_m required to establish the complete zig-zag feature scales with the twist angle (Fig. 4), since the bias needed to fully fill the moiré surface band grows with increasing twist angle.

QOs projecting to full filling ($\nu = \pm 4$) are evident in all devices shown in Fig. 4 except for the t1+40 device. The twist angle for the t1+40 device was instead estimated through piezoelectric force microscopy (PFM) imaging of the moiré pattern (Supplementary Information Fig. S2). PFM was performed on the transfer slide during the sample fabrication directly after picking up the 40-layer graphite and the monolayer graphene [40]. The twist angle is extracted by calculating the average of the three moiré lattice points in the Fourier transform of the PFM image. The twist angle in the t1+6 device was also independently confirmed in this manner.

When observed, the BZ oscillation sequence provides an independent measure of the twist angle. Magnetoconductance peaks are expected to occur when the magnetic flux $\phi = 4B/n_s$ is equal to p/q times the flux quantum $\phi_0 = h/e$, where h is Planck's constant and p, q are integers. We extract n_s by fitting the observed peaks to a series of rational $\phi/\phi_0 = 1/2, 1/3, 1/4$, etc. In all devices, we find that this value agrees with that extracted by tracking the QOs to within a few percent.

Low-field zig-zag behavior in the Hall resistance. In the main text, we describe the origin of the zig-zag behavior seen in the longitudinal resistance of the moiré graphite samples at low field. Here, we further describe the origin of a similar pattern in the Hall resistance. As seen in Fig. 2b, for $V_{gr} \approx 0$, the sign of the Hall effect flips as V_m is tuned. This occurs as the doping at the moiré surface switches between electron- and hole-like, corresponding to instances in which Fermi energy crosses a moiré band extrema or a Lifshitz transition. The origin of these sign changes can be understood in more detail by examining calculations of the constant-energy contours of the surface-localized moiré bands (Fig. 2c). We color-code these contours according to the sign of the local band curvature, and see a repeated switching of the free carrier type between hole-like, neutral, and electron-like as the energy of the bands is varied.

For sufficiently large values of V_{gr}, the doping of the Bernal graphite surface exceeds the maximum doping possible in the narrow moiré bands, and the sign of the Hall effect can no longer flip upon further biasing V_m. In Supplementary Information Fig. S9, we show that we can capture the salient features of this zig-zag effect following very simple assumptions about the amount of doping in each surface-localized band.

Temperature dependence measurements. We track the evolution of the low-field magnetotransport in the t1+17 device in Supplementary Information Fig. S3. We see signatures of the zig-zag feature persisting up to at least 50 K. As the temperature is raised further, the structure in the R_{xx} map becomes washed out. R_{xy} continues to exhibit a sign change, but along a straight line with a slope that becomes more vertical in the map with higher temperature. At room temperature, transport is nearly unaffected by changing V_m, potentially due to lower mobility on the moiré surface compared to the Bernal graphite surface.

Fitting the quantum oscillation sequences. To determine the zero-field projection points of the QOs, we first take the second derivative of the R_{xx} signal numerically. QOs manifest as resistance dips in the R_{xx} measurements, and are therefore peaks in the second derivative. The raw data and second derivative for a representative Landau fan from the t1+10 device is shown in Extended Data Fig. 5a-b. For clarity, we saturate the color scale to only show positive values of d^2R_{xx}/dV^2. We then identify QOs that persist over a magnetic field range of at least a tesla by determining linear trajectories in which d^2R_{xx}/dV^2 is a local maximum. We additionally cross check that the identified maxima in d^2R_{xx}/dV^2

correspond to obvious QO features in R_{xx}, since maxima in the second derivative can occasionally have other origins, such as two intersecting QOs or a QO crossing a BZ oscillation.

We then perform two different fitting procedures, which we refer to as "unconstrained" and "constrained" fits. For the unconstrained fit, we first perform a linear regression for each QO to extract its projection point at zero field, V_i^{u}. We can then group the QOs based on their projection points, forming groups that have projection points within a sufficiently small range of gate voltage. Extended Data Figs. 5c and e show an example of this analysis for the t1+10 device, in which V_{gr} was swept while fixing $V_m = 0$. We find two distinct sets of QOs, one that projects to approximately $V_{gr} = 0$ (associated with graphite surface states) and another to $V_{gr} \neq 0$ (associated with the extended bulk states). The linear regression fit to each QO has an associated error on its projection point, σ_i. These are shown as the colored data points with error bars in Extended Data Figs. 5g-h (collectively shown in the pink shaded region of the plot). After forming two groups of QOs based on their distinct projection points of $V_{gr} \approx 0$ and $V_{gr} \approx 0.02$ V/nm, we take a weighted average of all the QO projection points in each group in order to determine a single value for the projection point along with an associated error. The weights are $w_i = 1/\sigma_i^2$, such that the final projection point determined by the unconstrained fit is

$$\overline{V_0^u} = \frac{\sum_i w_i V_i^u}{\sum_i w_i}.$$

We assign the error to the unconstrained fit result as a weighted standard deviation:

$$\overline{\sigma^u} = \frac{1}{\sum_i w_i} \sqrt{\sum_i w_i^2 \left(V_i - \overline{V_0^u}\right)^2}.$$

The extracted $\overline{V_0^u}$ are denoted as vertical lines in Fig. 5g-h, with the surrounding shaded gray region indicating the fitting error. The unconstrained fits reveal two distinct sets of QOs with clearly distinguishable V_{gr} projection points. We stress that this fitting procedure is completely unbiased, as it simply picks out extended linear maxima in d^2R_{xx}/dV^2 and tracks their zero-field projection without making any underlying physical assumptions regarding the origin of those features.

We can strengthen this analysis by assuming that each distinct set of QOs must have the same projection point, as is conventional for quantum Hall states forming a Landau fan diagram. We thus proceed with a constrained fit, in which we additionally enforce a single projection point for each set of QOs, V_0^c. We further enforce that the QOs are related to one another through a Diophantine equation,

$$B = \frac{m}{t}\left(V - V_0^c\right),$$

where t is an integer (i.e. the Chern number) and $m = C\Phi_0/e$, with C the capacitance per unit area of the BN dielectric, e the charge of the electron, and $\Phi_0 = h/e$ the magnetic flux quantum. We use the results of the unconstrained fit to inform our assignment of the value of t for each fitted QO. We then perform a least squares regression to determined V_0^c and find the associated error, σ^c. In the Landau fans acquired by sweeping V_m, the difference between the fitted projection points associated with charge neutrality, $V^c_{0,\nu=0}$, and full-filling, $V^c_{0,\nu=\pm4}$, can be related to the moiré superlattice density, n_s, following $V^c_{0,\nu=\pm4} - V^c_{0,\nu=0} = \pm\frac{en_s}{C_m}$. Representative constrained fits are shown in Extended Data Figs. 5d and f.

The results of the constrained fit, V_0^c, are plotted as the black dots in Extended Data Figs. 5g-h (shown within the blue shaded region of the plot). These black dots and associated error correspond very closely to the black lines and associated error from the unconstrained fits, indicating that the two procedures yield highly consistent results. Given the physically realistic assumptions in the constrained fit, we adopt this procedure and further fit the projection points of the QO sequences from the remainder of the Landau fans acquired in this work. All data points shown in Fig. 3 report fits of V_0^c along with associated error bars, although the latter are typically smaller than the size of the corresponding data point marker. Extended Data Figs. 8, 9, and 10 further show further results from the constrained fitting procedure for representative Landau fans acquired in the t1+10, t1+17, and t1+6 devices, respectively.

Finally, we note that in some cases we are able to identify additional sequences of QOs beyond those discussed in the main text (detailed in Supplementary Information Fig. S5). In particular, we find these in Landau fans acquired by sweeping V_{gr} in the t1+10 and t1+17 devices. We do not know the origin of these additional states, although we find that they are extremely sparse compared with those comprising the two primary sequences of QOs that we fit. These additional QO sequences could be related to Hofstadter states that penetrate deep into the bulk, or could arise from another unknown origin.

Transport model of Bernal graphite at low field. We capture the low-field transport behavior of Bernal graphite with a four-component Drude model. Magnetotransport is characterized by the conductivity tensor $\boldsymbol{\sigma}$, with a corresponding current density $\boldsymbol{j} = \boldsymbol{\sigma}\boldsymbol{E}$ under an electric field $\boldsymbol{E}$. Each of the four carrier species are independent, and have a two-dimensional carrier density denoted as n_i, where i is t, b, e, or h. In order, these correspond to the charges on the top and bottom graphite surfaces, and the intrinsic electron and hole free carriers in the graphite bulk. Each carrier species has an associated mobility, μ_i. In the absence of a magnetic field, the conductivity is a scalar and the contribution from the i-th carrier is $\sigma_i = en_i\mu_i$. In the presence of a magnetic

field, the conductivity tensor is $\boldsymbol{\sigma} = \sum_i \boldsymbol{\sigma}_i$ where the contribution from the i-th carrier is

$$\boldsymbol{\sigma}_i = \frac{\sigma_i}{1+(\mu_i B)^2}\begin{pmatrix} 1 & \eta_i\mu_i B \\ -\eta_i\mu_i B & 1 \end{pmatrix},$$

with $\eta_i = \mp 1$ for electrons and holes, respectively. The resistivity tensor is $\boldsymbol{\rho} = \sigma^{-1}$, where the diagonal and off-diagonal elements separately represent the longitudinal (ρ_{xx}) and transverse (ρ_{xy}) resistivities.

Graphite is a nearly compensated semimetal, and for simplicity we assume $n_e = n_h$. We take previously measured parameters of bulk graphite [25, 41], in which the three-dimensional bulk carrier density is $n_{3\mathrm{D}} = 3 \times 10^{18}$ cm^{-3} and the mobility is $\mu_e = \mu_h = 1 \times 10^6$ cm^2/Vs. We assume the same value for the surface mobilities, μ_t and μ_b. The bulk electron and hole carrier densities correspond to a two-dimensional density of $n_{2\mathrm{D}} = 2 \times 10^{12}$ cm^{-2} per graphene sheet. To model our 23-layer Bernal graphite sample, we assign 21 layers of $n_{2\mathrm{D}}$ as the fixed bulk density, $n_e = n_h = 21 \times n_{2\mathrm{D}} = 4 \times 10^{13}$ cm^{-2}. We then vary the surface density of the two remaining layers, corresponding to changing the top and bottom gate voltages over typical experimentally accessible values.

Supplementary Information Fig. S8a shows the results of the calculation, which qualitatively match the experimental observations in Fig. 2a. In particular, we see the largest resistivity along the line of overall charge neutrality, with a corresponding change in the sign of the Hall effect. We also see that the resistivity is largest when both of the surfaces are undoped, also consistent with our experimental results. The qualitative agreement between experiment and theory does not depend strongly on the precise values of the graphite parameters we assume. However, as an additional check, we repeat the calculation with unrealistically large bulk density, $n_e = n_h = 2 \times 10^{15}$ cm^{-12} (Supplementary Information Fig. S8b). In this case, we find that virtually no gate dependence can be observed in the longitudinal resistivity, which changes by only tenths of an ohm, compared to over a hundred ohms in the calculation performed with realistic graphite parameters. These calculations therefore establish that the gate-tunable transport we observe in graphite arises as a consequence of its modest intrinsic bulk doping.

Band structure calculation. We first calculate the Hamiltonian for Z-layer Bernal graphite. We define $|\boldsymbol{k}, A_l\rangle$ and $|\boldsymbol{k}, B_l\rangle$ as the Bloch states at the K point of layer l. By arranging the basis as $|\boldsymbol{k}, A_1\rangle, |\boldsymbol{k}, B_1\rangle; |\boldsymbol{k}, A_2\rangle, |\boldsymbol{k}, B_2\rangle; ...; |\boldsymbol{k}, A_Z\rangle, |\boldsymbol{k}, B_Z\rangle;$, the Hamiltonian around the K point is given by

$$H_{\mathrm{ZG}}(\boldsymbol{k}) = \begin{pmatrix} H_{\mathrm{D}}(\boldsymbol{k}) - U_1 & \Gamma(\boldsymbol{k}) & 0 & \\ \Gamma^\dagger(\boldsymbol{k}) & H_{\mathrm{D}}(\boldsymbol{k}) - U_2 & \Gamma^\dagger(\boldsymbol{k}) & \\ 0 & \Gamma(\boldsymbol{k}) & H_{\mathrm{D}}(\boldsymbol{k}) - U_3 & \\ & & & \ddots \end{pmatrix},$$

with

$$H_{\mathrm{D}}(\boldsymbol{k}) = \begin{pmatrix} 0 & \frac{\sqrt{3}}{2}\gamma_0(k_x - ik_y) \\ \frac{\sqrt{3}}{2}\gamma_0(k_x + ik_y) & 0 \end{pmatrix},$$

and

$$\Gamma(\boldsymbol{k}) = \begin{pmatrix} -\frac{\sqrt{3}}{2}\gamma_4(k_x - ik_y) & -\frac{\sqrt{3}}{2}\gamma_3(k_x + ik_y) \\ \gamma_1 & -\frac{\sqrt{3}}{2}\gamma_4(k_x - ik_y) \end{pmatrix},$$

where U_j is the electronic potential at jth layer. We set the parameters $(\gamma_0, \gamma_1, \gamma_3, \gamma_4) = (2.6, 0.36, 0.28, 0.14)$ eV [42].

To calculate the band structure of twisted graphene-graphite, we further place a single graphene layer on the Z-layer graphite and twist it by θ. The effective Hamiltonian can be written as

$$H = \begin{pmatrix} H_{\mathrm{MG}} & H_{\mathrm{int}}^\dagger \\ H_{\mathrm{int}} & H_{\mathrm{ZG}} \end{pmatrix},$$

where H_{MG} is the Hamiltonian for the twisted monolayer graphene. H_{int} is the interlayer coupling term between the monolayer and the topmost layer of the graphite. We define $|\boldsymbol{k}', A_0\rangle$ and $|\boldsymbol{k}', B_0\rangle$ as the Bloch states of the twisted graphene at $R(\theta)K$, where $R(\theta)$ is the rotation matrix in the xy-plane at an angle θ. By using this basis, the Hamiltonian for the graphene can be represented as

$$H_{\mathrm{MG}} = \begin{pmatrix} U_0 & \frac{\sqrt{3}}{2}\gamma_0(k'_x - ik'_y) \\ \frac{\sqrt{3}}{2}\gamma_0(k'_x + ik'_y) & U_0 \end{pmatrix}.$$

The Bloch wavevector of the twisted graphene and the Z-layer graphite are coupled when $\boldsymbol{k} = \boldsymbol{k}' + \boldsymbol{q}_j$ ($j = 0, 1, 2$), where $\boldsymbol{q_0} = (0, 0)$, $\boldsymbol{q}_1 = \frac{1}{L_M}(-\frac{2\pi}{\sqrt{3}}, -2\pi)$ and $\boldsymbol{q}_2 = \frac{1}{L_M}(\frac{2\pi}{\sqrt{3}}, -2\pi)$, where L_M is the moiré lattice constant. Under these constraints, the interlayer coupling is given by

$$H_{int} = \sum_{j=0}^{2} t_{int}\begin{pmatrix} \alpha & e^{-i\frac{2\pi j}{3}} \\ e^{i\frac{2\pi j}{3}} & \alpha \end{pmatrix},$$

and is otherwise zero. We take the parameters $t_{int} = 0.11$ eV and $\alpha = 0.5$ [43], the latter of which captures the effects of lattice relaxations.

We additionally consider the effective model for Z-layer graphite twisted atop Z-layer graphite, such that the moiré interface is buried at the center of the material. The Hamiltonian is constructed following same analysis as above, but replacing H_{MG} with $H_{\mathrm{ZG}}(\boldsymbol{k}')$. The two rotated graphite constituents are coupled by H_{int} at their rotated interface.

We capture the effects of gating by adopting the Thomas-Fermi approximation to account for the screening of external electric fields by the graphite bulk [44, 45]. For small gate voltages, the electric field is given by

$$U_j = U_m e^{-jd/\lambda_s} + U_{gr} e^{-(Z-j)d/\lambda_s} \quad (j = 0, ..., Z)$$

where $\lambda_s \approx 1.3d$, and d is the interlayer distance. $U_{m/gr}$ is the potential for the moiré/graphite surface.

Finally, we numerically calculate the eigenvalues and eigenstates by truncating at a sufficiently large momentum and diagonalizing the Hamiltonian. The electron of the n-th eigenvalue is distributed along the graphite c-axis as follows:

$$\langle z_{n\boldsymbol{k}} \rangle = \sum_{l} \sum_{\sigma=A,B} z_l |\phi_{n\boldsymbol{k},\sigma_l}|^2$$

where the eigenstate is written as $|\psi_{n\boldsymbol{k}}\rangle = \sum_{\sigma,l} \phi_{n\boldsymbol{k},\sigma_l} |\boldsymbol{k}, \sigma_l\rangle$ and $z_l = 2(z_0 - ld)/L_z$. L_z and z_0 denote the width and the center of the system, respectively. Supplementary Information Figs. S6 and S7 provide a more detailed analysis of these band structure calculations.

DATA AVAILABILITY

Source data are available for this paper. All other data that support the findings of this study are available from the corresponding author upon request.

ACKNOWLEDGMENTS

We thank D. Cobden, V. Fal'ko, S. Slizovskiy, and M. Rudner for valuable discussions. This work was supported by NSF CAREER award DMR-2041972 and NSF MRSEC 1719797. M.Y. acknowledges support from the State of Washington funded Clean Energy Institute. D.W. was supported by an appointment to the Intelligence Community Postdoctoral Research Fellowship Program at University of Washington administered by Oak Ridge Institute for Science and Education (ORISE) through an interagency agreement between the U.S. Department of Energy and the Office of the Director of National Intelligence (ODNI). E.T. and E.A-M. were supported by NSF GRFP DGE-2140004. Electrical transport calculations were supported by the Department of Energy, Basic Energy Sciences, Materials Sciences and Engineering Division, Pro-QM EFRC (DE-SC0019443). M.F. was supported by JST CREST Grant Number JPMJCR20T3 and by JSPS KAKENHI Grants No. JP21J10775 and JP23KJ0339. K.W. and T.T. acknowledge support from the Elemental Strategy Initiative conducted by the MEXT, Japan (Grant Number JPMXP0112101001) and JSPS KAKENHI (Grant Numbers 19H05790, 20H00354 and 21H05233). This research acknowledges usage of the millikelvin optoelectronic quantum material laboratory supported by the M. J. Murdock Charitable Trust.

AUTHOR CONTRIBUTIONS

D.W., E.T. and E.A-M. fabricated the devices and performed the measurements. M.F. performed the band structure calculations. Y.R. performed the magneto-transport calculation. T.C. and D.X. supervised the calculations. K.W. and T.T. grew the BN crystals. D.W., E.T., E.A.-M. and M.Y. analyzed the data and wrote the paper with input from all authors.

COMPETING INTERESTS

The authors declare no competing interests.

ADDITIONAL INFORMATION

Correspondence and requests for materials should be addressed to M.Y.

SUPPLEMENTARY INFORMATION

Supplementary Information Figures S1-S9 and Supplementary Videos S1-S5.

REFERENCES

[1] Balents, L., Dean, C. R., Efetov, D. K. & Young, A. F. Superconductivity and strong correlations in moiré flat bands. *Nature Physics* **16**, 725–733 (2020).

[2] Andrei, E. Y. & MacDonald, A. H. Graphene bilayers with a twist. *Nature Materials* **19**, 1265–1275 (2020).

[3] Bistritzer, R. & MacDonald, A. H. Moiré bands in twisted double-layer graphene. *Proceedings of the National Academy of Sciences* **108**, 12233–12237 (2011).

[4] Suárez Morell, E., Correa, J. D., Vargas, P., Pacheco, M. & Barticevic, Z. Flat bands in slightly twisted bilayer graphene: Tight-binding calculations. *Physical Review B* **82**, 121407(R) (2010).

[5] Cao, Y. *et al.* Correlated insulator behaviour at half-filling in magic-angle graphene superlattices. *Nature* **556**, 80–84 (2018).

[6] Cao, Y. *et al.* Unconventional superconductivity in magic-angle graphene superlattices. *Nature* **556**, 43–50 (2018).

[7] Lu, X. *et al.* Superconductors, orbital magnets, and correlated states in magic angle bilayer graphene. *Nature* **574**, 653–657 (2019).

[8] Yankowitz, M. *et al.* Tuning superconductivity in twisted bilayer graphene. *Science* **363**, 1059–1064 (2019).

[9] Park, J. M., Cao, Y., Watanabe, K., Taniguchi, T. & Jarillo-Herrero, P. Tunable strongly coupled superconductivity in magic-angle twisted trilayer graphene. *Nature* **590**, 249–255 (2021).

[10] Hao, Z. *et al.* Electric field tunable superconductivity in alternating-twist magic-angle trilayer graphene. *Science* **371**, 1133–1138 (2021).

[11] Park, J. M. *et al.* Robust superconductivity in magic-angle multilayer graphene family. *Nature Materials* **21**, 877–883 (2022).

[12] Burg, G. W. *et al.* Emergence of correlations in alternating twist quadrilayer graphene. *Nature Materials* **21**, 884–889 (2022).

[13] Zhang, Y. *et al.* Promotion of superconductivity in magic-angle graphene multilayers. *Science* **377**, 1538–1543 (2022).

[14] Chen, S. *et al.* Electrically tunable correlated and topological states in twisted monolayer–bilayer graphene. *Nature Physics* **17**, 374–380 (2021).

[15] Polshyn, H. *et al.* Electrical switching of magnetic order in an orbital chern insulator. *Nature* **588**, 66–70 (2020).

[16] Shi, Y. *et al.* Tunable van hove singularities and correlated states in twisted monolayer-bilayer graphene. *Nature Physics* **17**, 619–626 (2021).

[17] He, M. *et al.* Competing correlated states and abundant orbital magnetism in twisted monolayer-bilayer graphene. *Nature Communications* **12**, 4727 (2021).

[18] Shen, C. *et al.* Correlated states in twisted double bilayer graphene. *Nature Physics* **16**, 520–525 (2020).

[19] Liu, X. *et al.* Tunable spin-polarized correlated states in twisted double bilayer graphene. *Nature* **583**, 221–225 (2020).

[20] Cao, Y. *et al.* Tunable correlated states and spin-polarized phases in twisted bilayer–bilayer graphene. *Nature* **583**, 215–220 (2020).

[21] Burg, G. W. *et al.* Correlated insulating states in twisted double bilayer graphene. *Physical Review Letters* **123**, 197702 (2019).

[22] He, M. *et al.* Symmetry breaking in twisted double bilayer graphene. *Nature Physics* **17**, 26–30 (2021).

[23] Cea, T., Walet, N. R. & Guinea, F. Twists and the electronic structure of graphitic materials. *Nano Letters* **19**, 8683–8689 (2019).

[24] Li, G. *et al.* Observation of van hove singularities in twisted graphene layers. *Nature Physics* **6**, 109–113 (2010).

[25] Soule, D. E. Magnetic field dependence of the hall effect and magnetoresistance in graphite single crystals. *Phys. Rev.* **112**, 698–707 (1958).

[26] Yin, J. *et al.* Dimensional reduction, quantum hall effect and layer parity in graphite films. *Nature Physics* **15**, 437–442 (2019).

[27] McClure, J. W. & Spry, W. J. Linear magnetoresistance in the quantum limit in graphite. *Phys. Rev.* **165**, 809–815 (1968).

[28] Hofstadter, D. R. Energy levels and wave functions of bloch electrons in rational and irrational magnetic fields. *Physical Review B* **14**, 2239 (1976).

[29] Brown, E. Bloch electrons in a uniform magnetic field. *Phys. Rev.* **133**, A1038–A1044 (1964).

[30] Hunt, B. *et al.* Massive dirac fermions and hofstadter butterfly in a van der waals heterostructure. *Science* **340**, 1427–1430 (2013).

[31] Dean, C. R. *et al.* Hofstadter's butterfly and the fractal quantum hall effect in moire superlattices. *Nature* **497**, 598–602 (2013).

[32] Ponomarenko, L. A. *et al.* Cloning of dirac fermions in graphene superlattices. *Nature* **497**, 594–597 (2013).

[33] Kumar, R. K. *et al.* High-temperature quantum oscillations caused by recurring bloch states in graphene superlattices. *Science* **357**, 181–184 (2017).

[34] Halbertal, D. *et al.* Multi-layered atomic relaxation in van der waals heterostructures. *arXiv:2206.06395* (2022).

[35] Zhou, H., Xie, T., Taniguchi, T., Watanabe, K. & Young, A. F. Superconductivity in rhombohedral trilayer graphene. *Nature* **598**, 434–438 (2021).

[36] Zhou, H. *et al.* Isospin magnetism and spin-polarized superconductivity in bernal bilayer graphene. *Science* **375**, 774–778 (2022).

[37] Chen, G. *et al.* Evidence of a gate-tunable mott insulator in a trilayer graphene moiré superlattice. *Nature Physics* **15**, 237–241 (2019).

[38] Saito, Y., Ge, J., Watanabe, K., Taniguchi, T. & Young, A. F. Independent superconductors and correlated insulators in twisted bilayer graphene. *Nature Physics* **16**, 926–930 (2020).

[39] Wang, L. *et al.* One-dimensional electrical contact to a two-dimensional material. *Science* **342**, 614–617 (2013).

[40] McGilly, L. J. *et al.* Visualization of moiré superlattices. *Nature Nanotechnology* **15**, 580–584 (2020).

[41] McClure, J. W. Analysis of multicarrier galvanomagnetic data for graphite. *Phys. Rev.* **112**, 715–721 (1958).

[42] Charlier, J.-C., Gonze, X. & Michenaud, J.-P. First-principles study of the electronic properties of graphite. *Physical Review B* **43**, 4579 (1991).

[43] Koshino, M. & Nam, N. N. T. Effective continuum model for relaxed twisted bilayer graphene and moiré electron-phonon interaction. *Physical Review B* **101**, 195425 (2020).

[44] Mañes, J. L., Guinea, F. & Vozmediano, M. A. H. Existence and topological stability of fermi points in multilayered graphene. *Phys. Rev. B* **75**, 155424 (2007).

[45] Koshino, M. Interlayer screening effect in graphene multilayers with *aba* and *abc* stacking. *Phys. Rev. B* **81**, 125304 (2010).

EXTENDED DATA

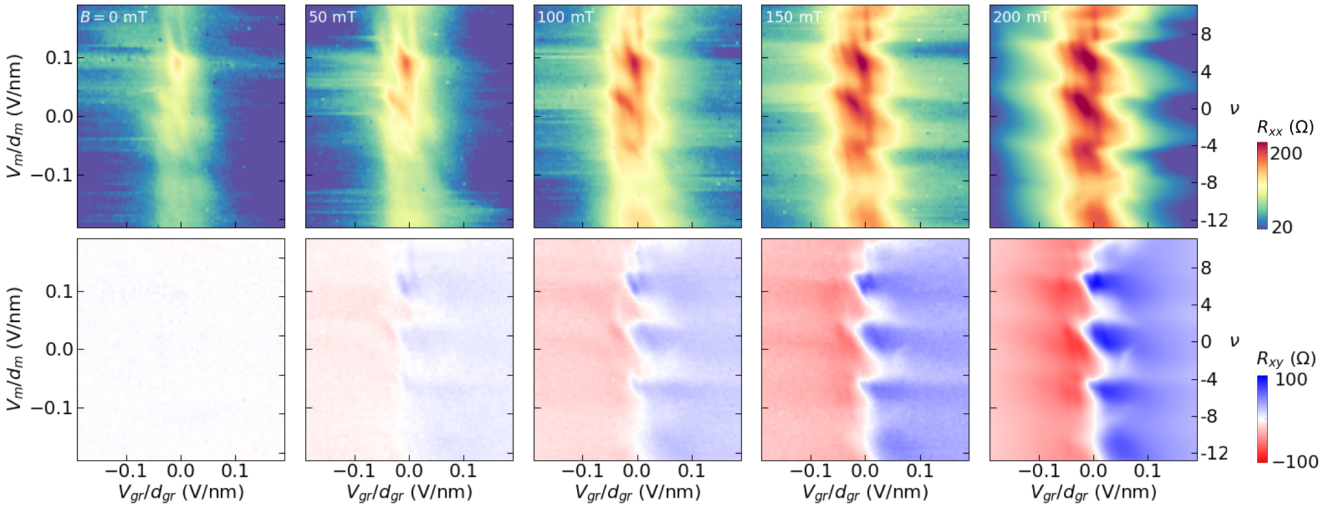

Extended Data Fig. 1. **Low-field evolution of transport in the t1+10 device.** Longitudinal (top) and Hall (bottom) resistance measurements acquired in steps of $B = 50$ mT, as indicated in the top left of each column. The zig-zag transport behavior first becomes evident at fields as low as 50 mT, and becomes more obvious as the field is raised.

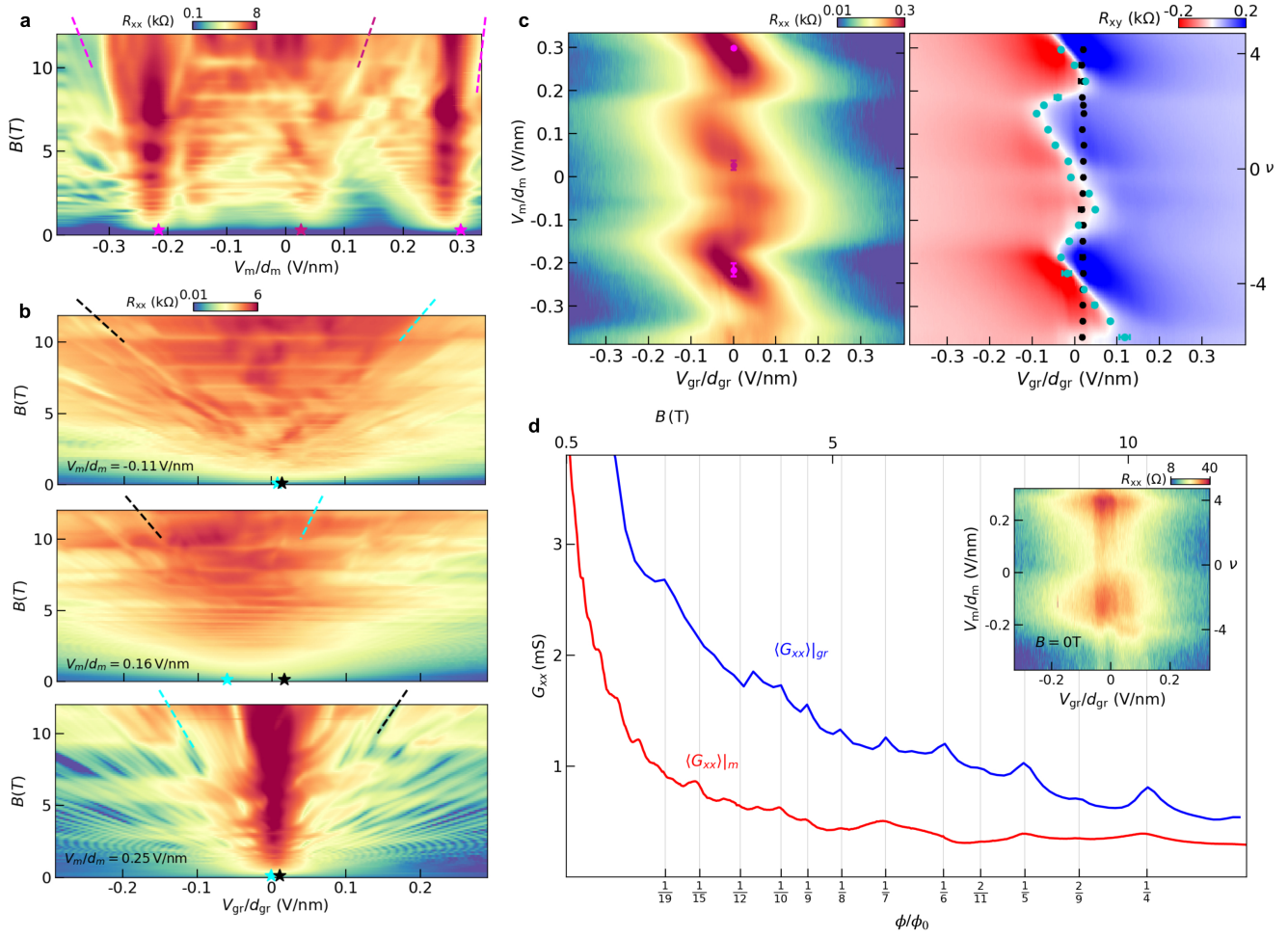

Extended Data Fig. 2. **High-field transport behavior in a t1+17 device with $\theta = 1.31°$. a**, Landau fan diagram acquired by sweeping V_m at $V_{gr} = 0$. The purple (pink) dashed lines denote selected QOs that project to $\nu = 0$ ($\nu = \pm 4$). **b**, Landau fan diagrams acquired by sweeping V_{gr} at various fixed values of V_m. The black dashed lines denote selected QOs that project to $V_{gr} \approx 0$ at $B = 0$. The blue lines denote selected QOs that project to a $V_{gr} \neq 0$ that depends on V_m. **c**, Longitudinal (left) and Hall (right) resistance maps acquired at $B = 0.5$ T. Zero-field projections of the $\nu = 0$ and ± 4 states from the V_m Landau fans are overlaid on the R_{xx} map. Zero-field projections of QOs from the V_{gr} Landau fans are overlaid on the R_{xy} map. **d**, Conductance, G_{xx}, as a function of magnetic field. The blue curve is averaged over all values of V_{gr} for the Landau fan in (**a**) acquired at $V_m/d_m = -0.11$ V/nm. The red curve is averaged over a range of V_m values corresponding to $|\nu| < 4$ for the Landau fan in (**b**) acquired at $V_{gr} = 0$. Brown-Zak oscillations case be seen upon sweeping either gate. (Inset) Longitudinal resistance map acquired at $B = 0$ T.

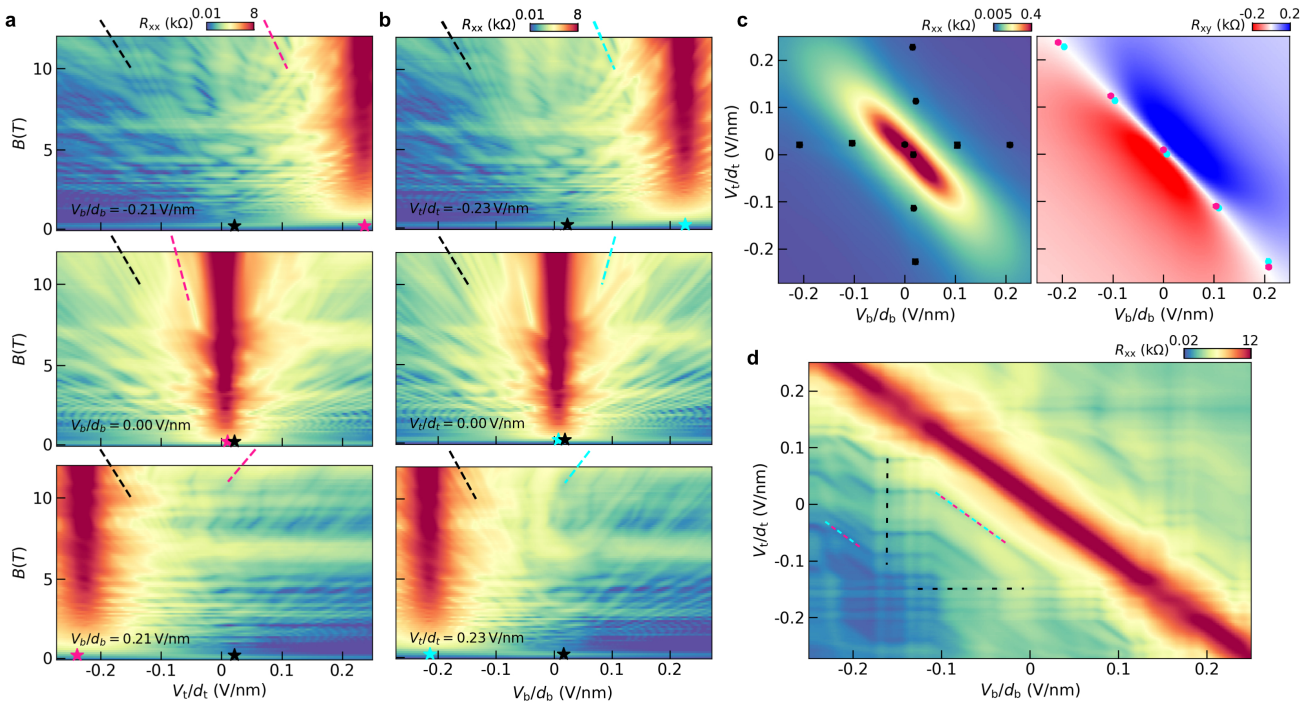

Extended Data Fig. 3. **High-field transport in Bernal graphite. a**, Landau fan diagrams from a 24-layer graphite device (different from the one shown in the main text) acquired by sweeping the top gate voltage, V_t, at various fixed values of the bottom gate voltage, V_b, as indicated in each panel. The black dashed lines denote selected QOs that project to $V_t \approx 0$ at $B = 0$, and the pink lines denote QOs that project to a $V_t \neq 0$ that depends on the value of V_b. **b**, Similar Landau fans, but with fixed V_t and sweeping V_b. The QOs projecting to $V_b \neq 0$ are denoted in blue. **c**, Longitudinal (left) and Hall (right) resistance maps acquired at $B = 0.5$ T. The QOs projecting to approximately zero gate voltage in each Landau fan, corresponding to surface-localized states, are overlaid on the R_{xx} map and form a cross. The QOs projecting to non-zero gate voltages, corresponding to extended bulk states, are overlaid on the R_{xy} map and closely track the condition of overall charge neutrality. **d**, R_{xx} map acquired at $B = 12$ T. Dashed black lines denote selected QOs that depend only on a single gate, which arise from localized states on either the top or bottom graphite surfaces. The blue/pink dashed lines denote QOs that depend on both gates, which evolve parallel to the line of overall charge neutrality, arising from the extended bulk states.

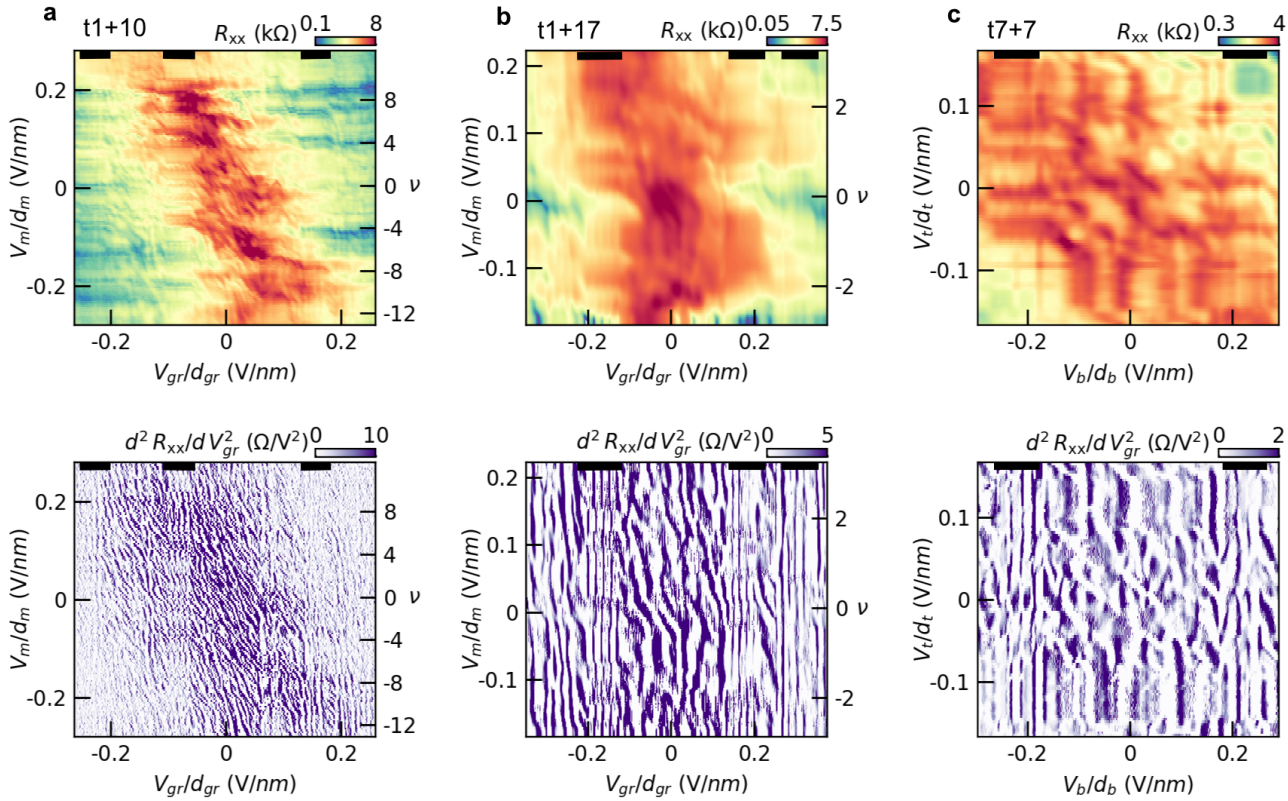

Extended Data Fig. 4. **High field dual-gate maps for the t1+10, t1+17, and t7+7 devices. a-c**, Dual-gate R_{xx} maps (top) and corresponding numerical second derivative (bottom) acquired for the (**a**) t1+10 device at $B = 9$ T, (**b**) t1+17 device at $B = 12$ T, and (**c**) t7+7 device at $B = 12$ T. Solid black bars at the top of each map denote regions of gate voltage dominated by vertical QOs, which correspond to surface-localized states. Other regions, though more complicated, contain diagonal QOs which depend on the value of both gate voltages. These features correspond to extended bulk standing wave states. Data in panel **a** was acquired in a dilution refrigerator with a nominal base temperature of $T \approx 20$ mK, all other data was acquired at 1.7 K.

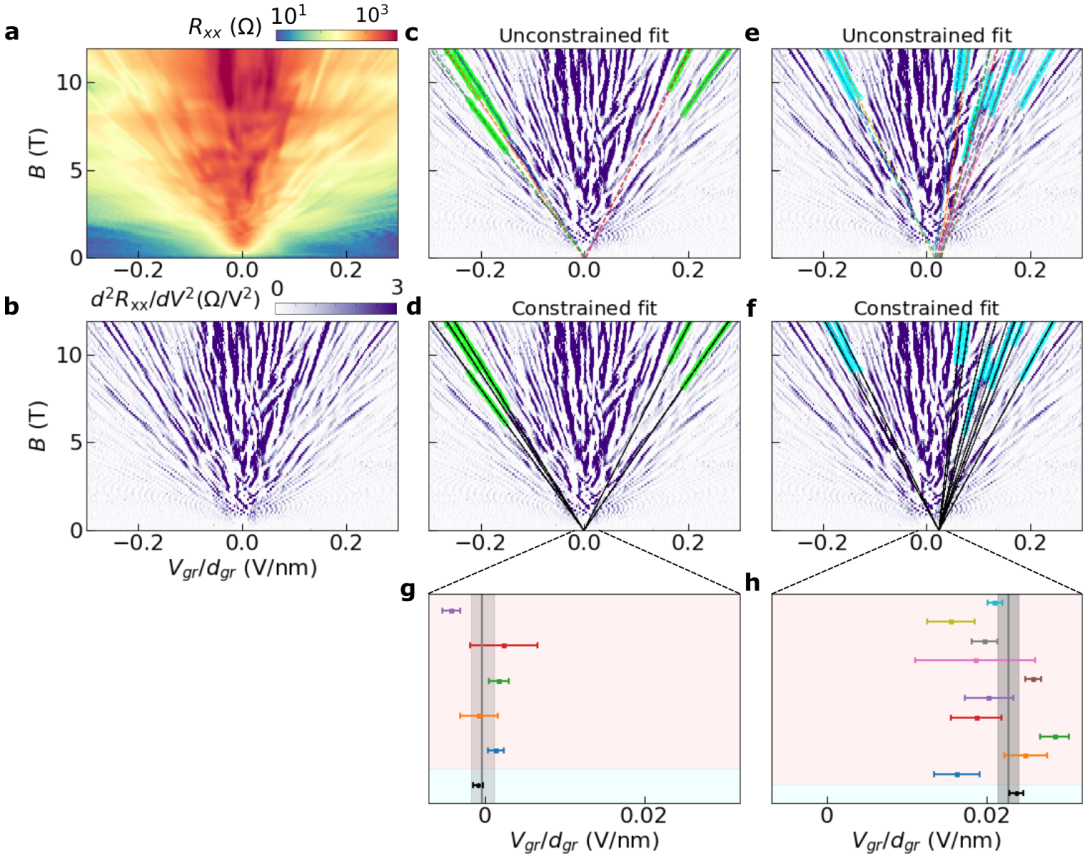

Extended Data Fig. 5. **Extracting the zero-field projection points of the QOs.** **a**, Landau fan diagram of R_{xx} in the t1+10 device, acquired by sweeping V_{gr} with $V_m = 0$. **b**, The numerical second derivative of the data in **a**. The color scale is saturated to only show positive values of d^2R_{xx}/dV^2, since peaks in d^2R_{xx}/dV^2 correspond to minima in R_{xx} (i.e., QOs). **c**, Fit results using the unconstrained fitting procedure for QOs that project to $V_{gr} \approx 0$. The green circles are extracted peaks in d^2R_{xx}/dV^2 that were used for each fit, and the dashed lines show the result of the fit for each individual QO. **d** Analogous results using the constrained fitting procedure for the QOs that project to $V_{gr} \approx 0$. The green data points are the same as in **c**, but now all the states are fit simultaneously and forced to share the same projection point at $B = 0$ with a defined relationship between their slopes (see Methods for full description). **e-f**, Similar fitting using the unconstrained and constrained fitting procedures, respectively, but for the sequence of QOs that project to $V_{gr} \neq 0$. **g**, Projection points determined from the fits shown in **c** and **d**. The shaded pink region contains data points and associated error bars from the unconstrained fit, $V_i^u \pm \sigma_i$, corresponding to the dashed lines in **c** of the same color. The vertical black line and surrounding shaded grey bar denote the weighted average and associated error of the unconstrained fit, $\overline{V_0^u} \pm \overline{\sigma^u}$. The shaded blue region contains the result of the constrained fit from **d**. The single black data point with error bars is the projection point determined by the constrained fit $V_0^c \pm \sigma^c$. Note that $\overline{V_0^u} \pm \overline{\sigma^u}$ and $V_0^c \pm \sigma^c$ are consistent with one another. **h**, Similar plot as **g**, but for the fits shown in **e** and **f**. Note that the extracted QO projection points in **g** and **h** differ significantly from one another, allowing us to unambiguously identify two distinct sets of QOs corresponding to the surface states and bulk states, respectively.

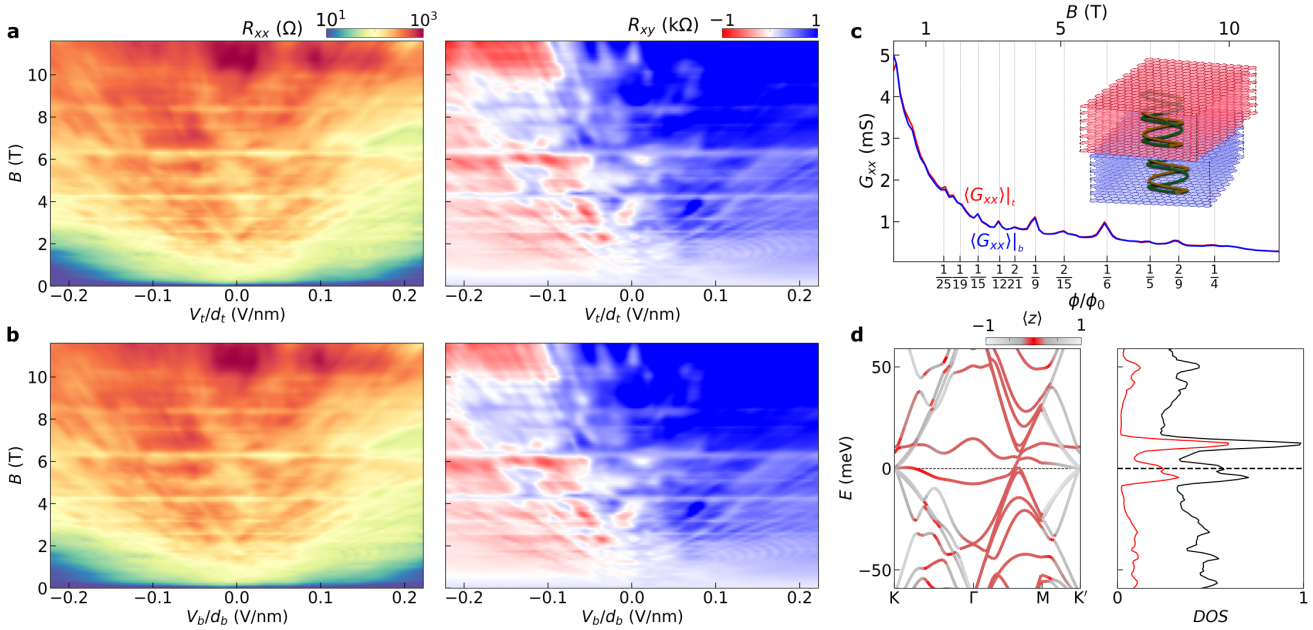

Extended Data Fig. 6. **High-field transport in a device with a buried moiré interface. a**, R_{xx} (left) and R_{xy} (right) Landau fans acquired as V_t is swept with $V_b = 0$ in a device consisting of 7 layers of Bernal graphite stacked and rotated atop another 7 graphite layers with $\theta = 1.26°$. **b**, Same as (**a**), but sweeping V_b with $V_t = 0$. The fans acquired by sweeping each gate are nearly identical to one another owing to the symmetry of the structure. Since the moiré is buried, we do not observe signatures of moiré band filling in either Landau fan. However, both fans show clear horizontal features corresponding to Brown-Zak oscillations arising from the buried moiré. **c**, Magnetoconductance averaged across all gate voltages for the top (red curve) and bottom (blue curve) gates. These are nearly identical, and both display a clear sequence of Brown-Zak oscillations. The inset shows a cartoon schematic in which separate standing waves couple the top and bottom bulk graphite states to the buried moiré interface. The hybridization of the buried moiré with the bulk states is required to generate the BZ oscillations seen in transport. **d**, (Left) Band structure calculation of this structure showing a moiré band localized at the center of the twisted graphitic thin film. The color scale is defined as in Fig. 2d of the main text. In this case, the moiré bands are found at $\langle z \rangle \approx 0$, since the moiré is located at the center of the structure. (Right) The density of states integrated over the moiré Brillouin zone. The red filtered curve corresponds to the four central graphene sheets, whereas the black corresponds to the total density of states.

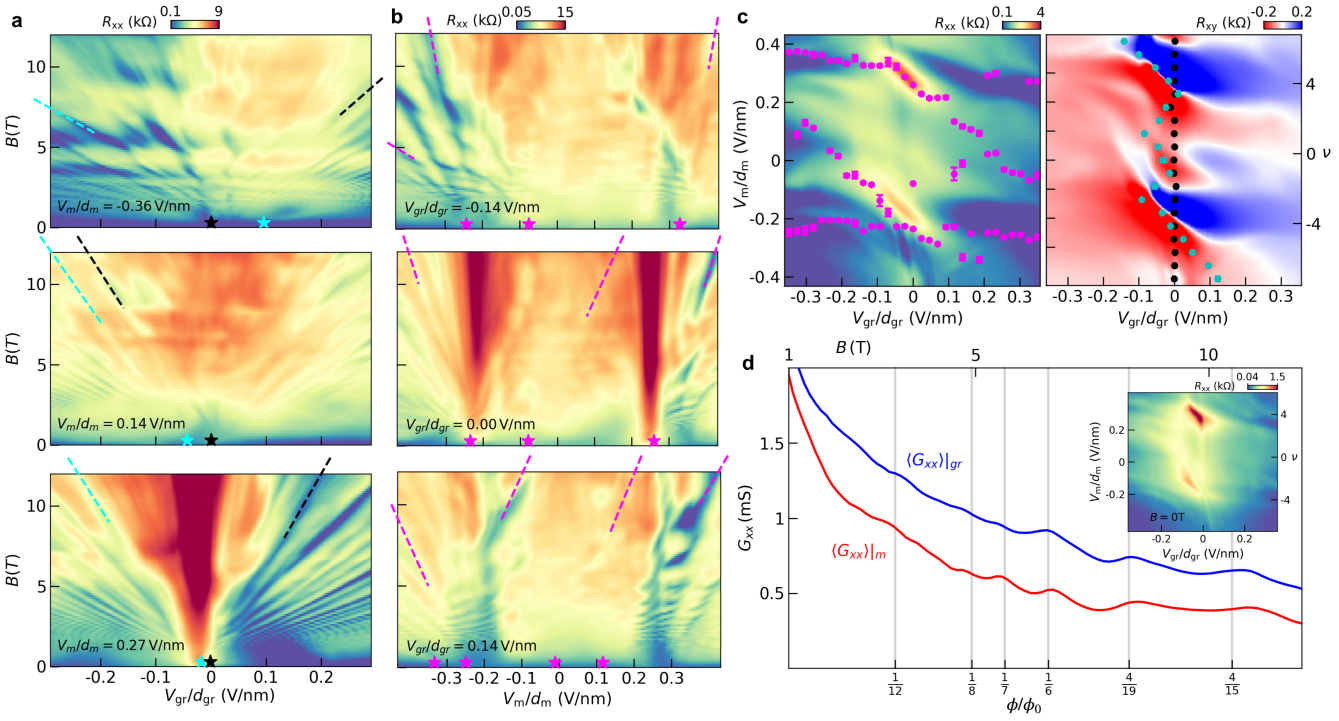

Extended Data Fig. 7. **High-field transport in a t1+6 device with $\theta = 1.27°$.** **a**, Landau fan diagrams acquired by sweeping V_{gr} at various fixed values of V_m. The black dashed lines denote selected QOs that project to $V_{gr} \approx 0$ at $B = 0$. The blue lines denote selected QOs that project to a $V_{gr} \neq 0$ that depends on V_m. **b**, Landau fan diagrams acquired by sweeping V_m at fixed values of V_{gr}. The pink dashed lines denote selected QOs from each of the distinct sequences we observe. **c**, Longitudinal (left) and Hall (right) resistance maps acquired at $B = 0.5$ T. Zero-field projections of all observed sequences of QOs from the V_m Landau fans are overlaid on the R_{xx} map. Zero-field projections of QOs from the V_{gr} Landau fans are overlaid on the R_{xy} map. We note that, in this device, the observed sequence of QOs in the V_m Landau fans is very complex, and there is not always a clear delineation between QO sequences arising from neutrality ($\nu = 0$) and full filling ($\nu = \pm 4$) of the moiré bands. This may be a consequence of the relatively thin nature of the sample, which exhibits features of both atomically-thin graphene and bulk graphite. Supplementary Information Fig. S4 further shows the dimensional crossover from 2D-like to 3D-like behavior as the number of graphene layers in the sample is increased.

d, Conductance, G_{xx}, as a function of magnetic field. The blue curve is averaged over all values of V_{gr} for the Landau fan acquired at $V_m/d_m = -0.05$ V/nm. The red curve is averaged over a range of V_m values corresponding to $|\nu| < 4$ for the Landau fan in **b** acquired at $V_{gr} = 0$. Brown-Zak oscillations case be seen upon sweeping either gate. (Inset) Longitudinal resistance map acquired at $B = 0$ T.

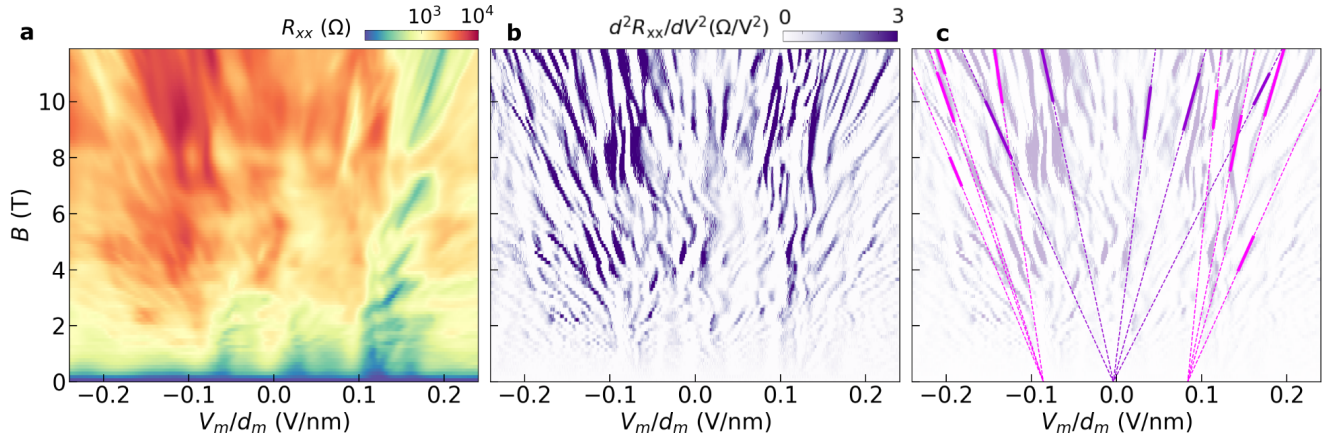

Extended Data Fig. 8. **Representative constrained fit results for Landau fans acquired by sweeping V_m in the t1+10 device.** **a**, Landau fan diagram of R_{xx} in the t1+10 device, acquired by sweeping V_m with $V_{gr}/d_{gr} = 0.01$ V/nm. **b**, Numerical second derivative of the data in **a**. The color scale is saturated to only show positive values, as in Extended Data Fig. 5. **c**, Results of the constrained fit overlaid on the second derivative data from **b**, with reduced opacity for clarity. Solid segments denote the range of magnetic field over which the QOs were fit, and the dashed segments denote the projection over the entire range of magnetic field.

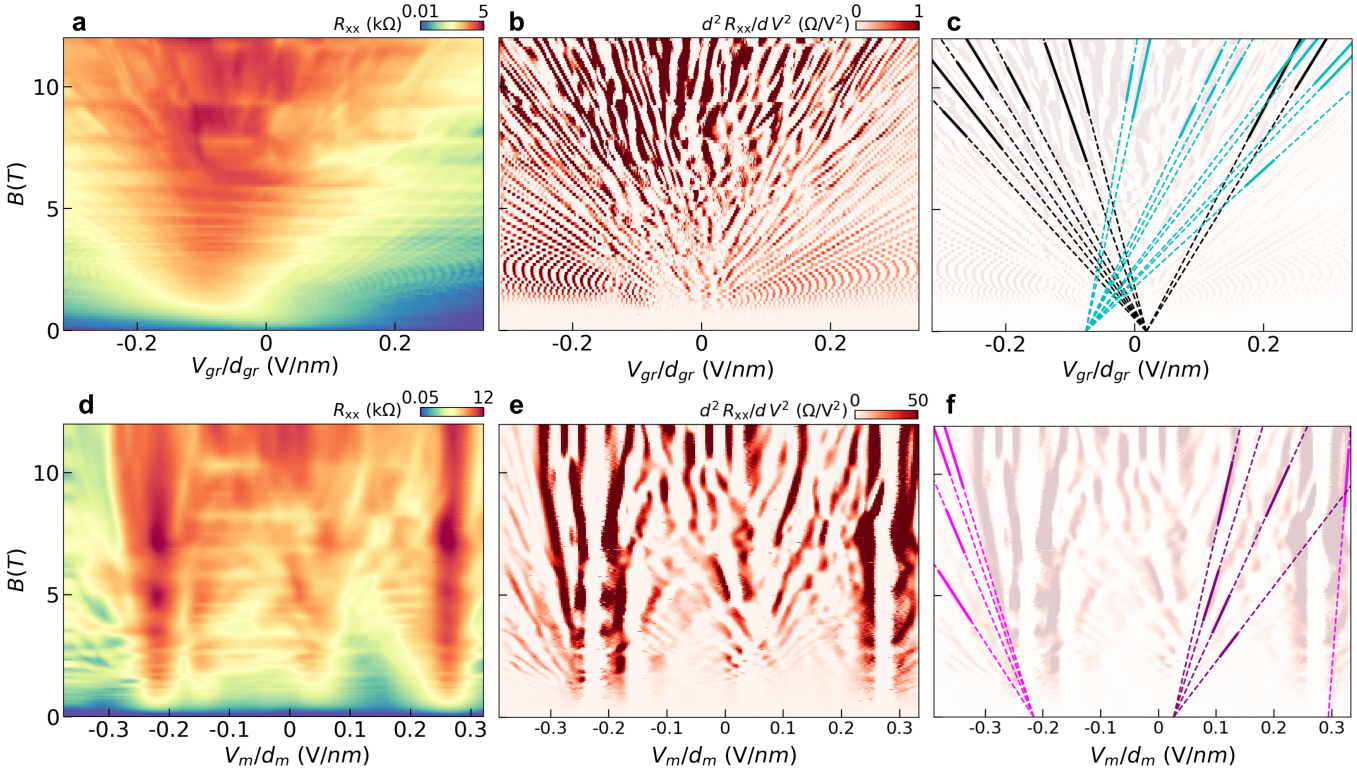

Extended Data Fig. 9. **Representative constrained fit results for the t1+17 device.** Same plots as in Extended Data Fig. 8, but for the t1+17 device. **a-c**, Landau fan acquired by sweeping V_{gr} with $V_m/d_m = 0.14$ V/nm, and associated QO fits. **d-e**, Landau fan acquired by sweeping V_m with $V_{gr}/d_{gr} = 0$, and associated QO fits.

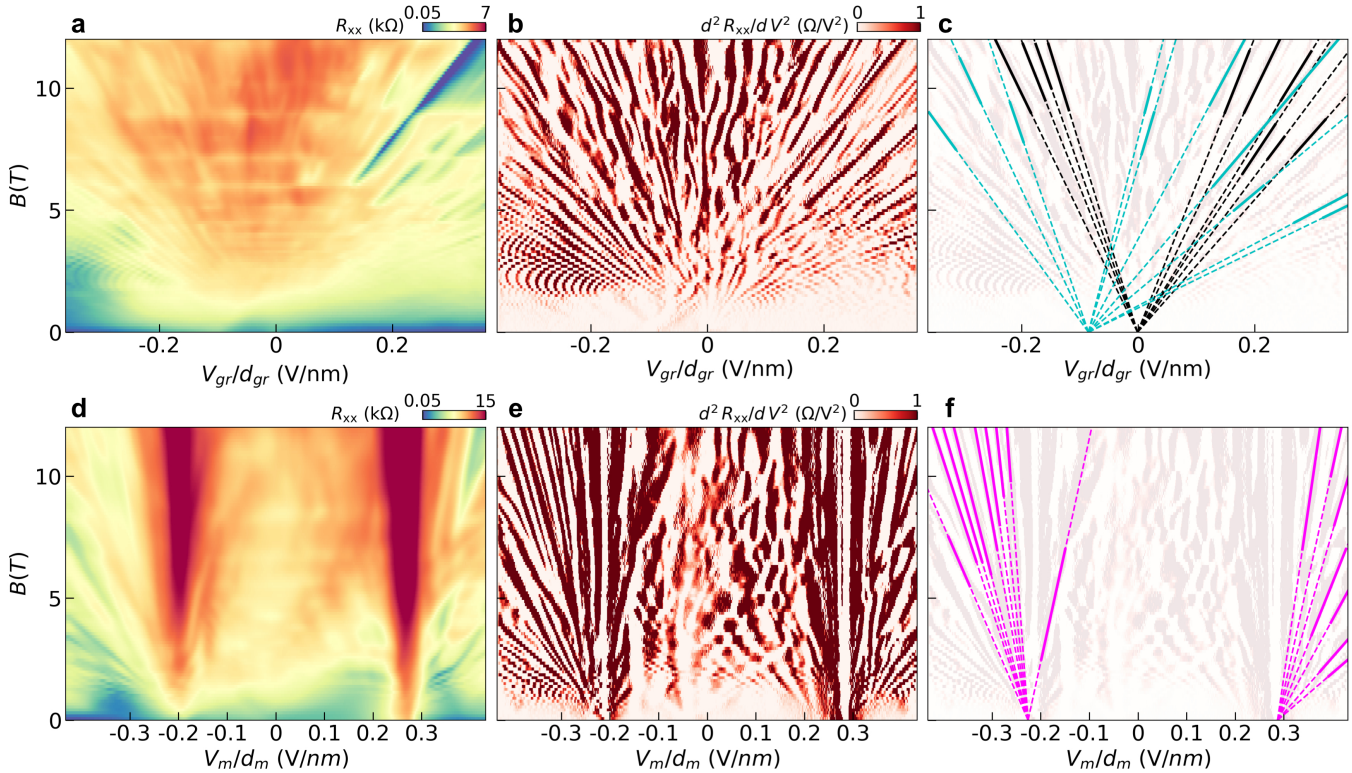

Extended Data Fig. 10. **Representative constrained fit results for t1+6 device.** Same plots as in Extended Data Fig. 8, but for the t1+6 device. **a-c**, Landau fan acquired by sweeping V_{gr} with $V_m/d_m = 0.09$ V/nm, and associated QO fits. **d-e**, Landau fan acquired by sweeping V_m with $V_{gr}/d_{gr} = -0.02$ V/nm, and associated QO fits.

SUPPLEMENTARY VIDEOS

Supplementary Video 1. (left) Landau fan diagrams from the t1+10 device acquired by sweeping V_{gr} at the indicated values of V_m. The black and blue dots correspond to the $B = 0$ projection points of the QO sequences, as described in the main text. In general, the blue dots align with the value of V_{gr} corresponding to the highest resistance over a wide range of B in the map. (right) R_{xy} map acquired at $B = 0.5$ T with the corresponding black and blue dots overlaid.

Supplementary Video 2. (left) Landau fan diagrams from the t1+10 device acquired by sweeping V_m at the indicated values of V_{gr}. The pink and purple dots correspond to the $B = 0$ projection points of the QO sequences, as described in the main text. (right) R_{xx} map acquired at $B = 0.5$ T with the corresponding pink ($\nu = 0$) and purple ($\nu = \pm 4$) dots overlaid.

Supplementary Video 3. Same as Supplementary Video 1, but for the t1+6 device.

Supplementary Video 4. Same as Supplementary Video 2, but for the t1+6 device.

Supplementary Video 5. Same as Supplementary Video 1, but for the t1+17 device. This video only includes Landau fans with $V_{gr}/d_{gr} \geq -0.18$ V/nm. The fans acquired for $V_{gr}/d_{gr} < -0.18$ V/nm were taken only up to $B = 5$ T due to technical constraints in those particular measurements, and are not included in the video for the sake of continuity. Nevertheless, these lower-field fans still enable unambiguous QO projections, as plotted on the R_{xx} map.